Chip

Research Article

PHOTONICS

DOI: 10.1016/j.chip.2023.100077

Deterministic relation between thermal-phonon dressings and a non-Hermitian multi-Fano interferences router in ion-doped microcrystals

Huanrong Fan[1,†], Faizan Raza[1,3,†], Anas Mujahid[1,†], Peng Li[2], Yafen Wang[1], Haitian Tang[1], Muhammad Usman[1], Bo Li[1,*], Changbiao Li[1,*] & Yanpeng Zhang[1,*]

[1]*Key Laboratory for Physical Electronics and Devices of the Ministry of Education & Shaanxi Key Lab of Information Photonic Technique, Xi'an Jiaotong University, Xi'an 710049, China* [2]*Center for Regenerative and Reconstructive Medicine, Med-X Institute, The First Affiliated Hospital of Xi'an Jiaotong University, Xi'an 710061, China* [3]*State Key Lab of Modern Optical Instrumentation, Centre for Optical and Electromagnetic Research, College of Optical Science and Engineering, International Research Center for Advanced Photonics, Zhejiang University, Hangzhou 310058, China*

[†]These authors contributed equally to this work.

[*]E-mails: libophy@xjtu.edu.cn (Bo Li), cbli@mail.xjtu.edu.cn (Changbiao Li), ypzhang@mail.xjtu.edu.cn (Yanpeng Zhang)

Cite as: Fan, H. et al. Deterministic relation between thermal-phonon dressings and a non-Hermitian multi-Fano interferences router in ion-doped microcrystals. *Chip* **3**, 100077 (2024).
https://doi.org/10.1016/j.chip.2023.100077

Received: 4 September 2023

Accepted: 24 November 2023

Published online: 25 November 2023

The multi-Fano interference, which is obtained through the simultaneous acquisition of bright and dark states in different phase transitions of Eu^{3+} : $BiPO_4$ (7 : 1, 6 : 1, 1 : 1, and 0.5 : 1) and Eu^{3+} : $NaYF_4$ (1 : 1/4) crystals, were reported in this work. Multidressed spontaneous four-wave mixing and multidressed fluorescence (multiorder) were adopted to optimize the strong photon–phonon nested dressing effect, which results in more obvious multi-Fano interference. Firstly, the multi-Fano is produced through interference in continuous and multibound states. Secondly, five multi-Fano dips are originated from the nested five dressings (one photon and four phonons) under symmetrical splitting of $^7F_1$ energy level. It is found that the pure H-phase (0.5 : 1) sample exhibits the strongest photon–phonon dressed effect (five Fano dips). Further, high-order non-Hermitian exceptional points in multi-Fano interference were investigated by adjusting the ratio of Rabi frequency to dephase rate through nested photon and phonon dressing. The experimental results are validated by theoretical simulations, which may be applied to designing optoelectronic devices such as non-Hermitian multi-Fano interferences (multichannel) router.

Keywords: Multi-Fano interferences, Thermal-phonon dressings, Non-Hermitian, Router

INTRODUCTION

In recent years, notablly surging research efforts have been paid on Fano resonance, owing to its extensive range of material applications within the realms of physical, chemical, and biological sciences[1–7]. Structures with Fano resonance have great application potential in the fields of hybrid photonics and nanophotonics, which involve the coupling of light with various particles and quasiparticles such as phonons, electrons, spin, excitons, and mechanical degrees of freedom[8]. In Fano interference, interference of a discrete quantum state with a continuum of states with the same energy contributes to the appearance of asymmetric line shapes in the measured excitation spectra, which can be characterized by a Fano 'shape' parameter, and this was first observed in experiments by exciting rare gas atoms to Rydberg states[9,10]. Fano lineshapes serve as essential spectroscopic indicators that provide quantitative insights into the structural and dynamic properties of physical objects, spanning from nuclei to three-dimensional solids and liquids.

In recent studies, special emphases have been laid upon exploring higher-order exceptional points (EPs)[11–13] and parity-time (PT) symmetric systems that involve alternating gain and loss[14–18]. These systems have shown potential for effectively controlling non-Hermitian multi-Fano interference. The applications of Fano resonance encompass various domains, including the utilization of linear and nonlinear dielectric nano resonators, two-dimensional (2D) materials[19–21], slow light optomechanical nanocavities[22], Dirac semiconductors with ultrafast dynamics of phase and topology[23], Fano-lasers and spacers[24,25], and Fano devices[26,27]. Fano-based devices are very sensitive to changes in geometry and the surrounding environment, there still exist big hurdles in its the implementation despite the fact that it is an important part of an effective sensor.

To address this challenge, the advantages of adopting rare earth ion doped crystals to advance integrated quantum circuits have been widely recognized. The lifetime, coherence time, and spectral resolution of

doped crystals such as Eu^{3+} : YPO_4, Pr^{3+} : Y_2SiO_5, and Eu^{3+} : $BiPO_4$ can be precisely controlled through the nonlinear process[28,29]. However, among them, Eu^{3+} : $BiPO_4$ tends to be the best candidate due to the longest coherence among other doped crystals owing to photon–phonon dressing[30–33]. The functional crystal of $BiPO_4$ exhibits three different crystal structures, namely, hexagonal phase (HP, space group: Po3121), low-temperature monoclinic phase (LTMP, space group: P21/n), and high-temperature monoclinic phase (HTMP, space group: P21/m)[34,35]. The phase transition of $BiPO_4$ from LTMP or HTMP to HP occurs by continuously doping Ln^{3+} ions. The current research is mainly focused on investigating the effective manipulation of the phase transition, which results in the identification of the novel phenomena of multi-Fano resonances controlled through photon–phonon interaction and multidressing effect. However, all of the spectral Fano interferences that have been previously reported involved a single Fano interference arising from the interaction between one continuous state and one bound state, which are solely caused by external photon dressing.

In this paper, the complex relationship between novel multi-Fano interference and phase transitions of ion-doped microcrystals (Eu^{3+} : $BiPO_4$/Eu^{3+} : $NaYF_4$) was reported. The experimental results show that each energy level of the $BiPO_4$ fine structure exhibits distinct lattice vibrations, resulting in different phonon frequencies. As a consequence, the number of dressing levels varies, leading to the observation of multi-Fano interferences. The evolution of five Fano interferences from a single Fano interference was observed by precisely controlling the interaction between a continuous state and multibound states with the adoption of laser power, temperature, and gate position (GP). In this work, single-laser excitation results in a single Fano dip caused by the self-dressing effect, whereas multidressing is generated from photon–phonon multi-Fano interference. The non-Hermitian-controlled higher-order EPs was realized, which can be defined by real and imaginary quantization alignment. The outcomes were applied to suggest a non-Hermitian multichannel router and show that broadband peak input fluorescence (FL) to multi-Fano output can be achieved. This study explores extensively into the correlation between thermal-phonon dressings and multi-Fano interference in ion-doped microcrystals, with potential applications in the development of optoelectronic devices.

RESULTS

Scheme for multi-Fano interferences In our experiment, the molar ratio (PO_4^{3-} : [Bi^{3+} + Eu^{3+}]) of doped ions is adjusted with different concentrations of Hexagonal (H) and monoclinic (M) phase to obtain different phase transitions of $BiPO_4$ nanocrystals (7 : 1, 6 : 1, 1 : 1, 0.5 : 1) as shown in Fig. S1(a–f) (See Supplementary materials for detailed physical images of the samples). The (7 : 1, 6 : 1, 1 : 1) $BiPO_4$ crystals with C_1 point group site symmetry has a proportion of M-phase, whereas the concentration of H-phase is high in (0.5 : 1) the $BiPO_4$ sample (C_2 symmetry), which results in more lattice-vibrating phonon[36,37]. The Eu^{3+} : $NaYF_4$ (YF_4^{3-} : [Na^{3+} + Eu^{3+}] = 1 : 1/4) exhibits pure H-phase with Cs symmetry. The transition between H-phase to M-phase has been achieved by increasing the phosphate ion (PO_4^{3-}) concentration in the Eu^{3+} : $BiPO_4$ system, while different crystal phases are synthesized by adjusting the pH values[38–42].

In the experiment, samples were held in a cryostat (CFM-102) with temperatures varying from 300 K (strong phonon dressing) to 77 K (weak phonon dressing) by flowing liquid nitrogen. The left and middle of Fig. 1a show crystal field (CF) splitting levels of Eu^{3+} : BPO_4 and Eu^{3+} : $NaYF_4$, respectively. The right of Fig. 1a shows photon-assisted CF splitting in Eu^{3+} : BPO_4/$NaYF_4$. The $^7F_1$ fine structure (J = 1) splits into three levels: $^7F_{1,\,MJ=-1}$ (587.3 nm), $^7F_{1,\,MJ=0}$ (592.3 nm), and $^7F_{1,\,MJ=+1}$ (597.3 nm) under the dressing and CF effect of $BiPO_4$. Fig. 1b illustrates the subenergy levels corresponding to the right of Fig.1a. Two dye lasers (narrow scan with a 0.04 cm^{-1} linewidth and broad scan with a 0.08 cm^{-1} linewidth, R610 dye) pumped by an injection-locked single-mode Nd : YAG laser (Continuum Powerlite DLS 9010, 10 Hz repetition rate, 5 ns pulse width) were employed to generate the two pumping fields $E_1(\omega_1)$ and $E_2(\omega_2)$. By exciting the Eu^{3+}:$BiPO_4$ crystal

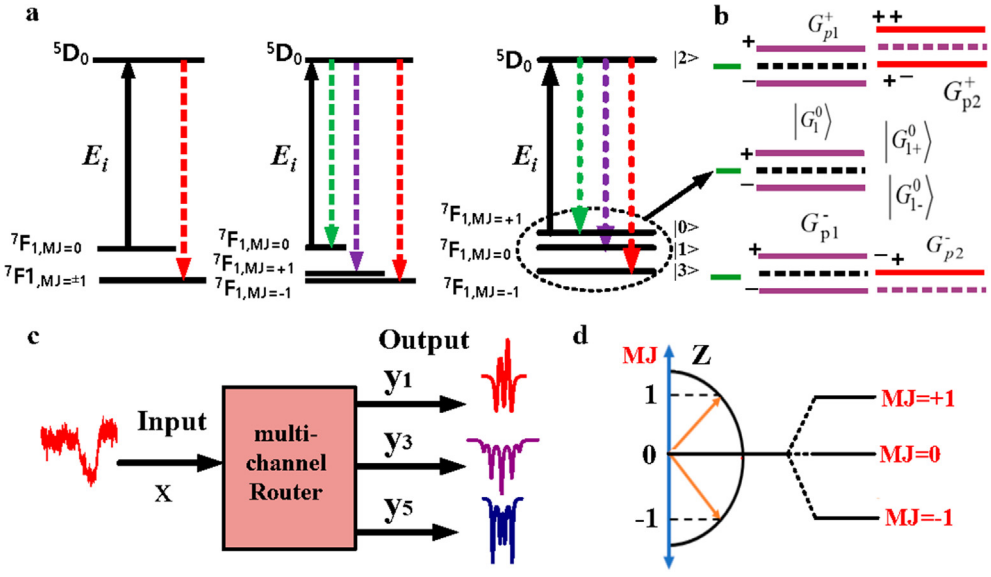

Fig. 1 | a, Energy level of ion-doped microcrystals and router. Crystal field splitting of $^7F_1$ energy level for Eu^{3+} : $BiPO_4$ (left) and Eu^{3+} : $NaYF_4$ (middle), respectively. Photon-assisted crystal filed splitting in Eu^{3+} : $BiPO_4$/$NaYF_4$ (right). **b,** Enlarged view of $^7F_1$ energy levels corresponding to **a**. **c,** Model of a non-Hermitian multichannel router. **d**, Dressing-like Zeeman splitting ($^7F_{1,\,MJ=-1}$, $^7F_{1,\,MJ=0}$ and $^7F_{1,\,MJ=+1}$) in Eu^{3+} : $BiPO_4$.

with $\boldsymbol{E_1}$ and $\boldsymbol{E}'_1$ (reflection of $\boldsymbol{E_1}$) (Fig. 1d), the output Stokes ($\boldsymbol{E_S}$)/anti-Stokes ($\boldsymbol{E_{AS}}$) signals are generated under a phase-matched condition ($K'_1 + K_1 = K_S + K_{AS}$) due to interaction with Eu^{3+} : $BiPO_4$ energy levels. The out-of-phase FL1 and FL2 are generated through $\boldsymbol{E_1}$ (broadband laser) and $\boldsymbol{E_2}$ (narrowband laser), respectively. The pulse generated from the Nd^{3+} : YAG laser is used to simultaneously trigger a boxcar-gated integrator (G) and oscilloscope (OS). The input laser beams are along the [010] axis of the crystal, which is perpendicular to the optical axis. The spectral optical outputs are obtained by scanning laser frequency, while the time-resolved OS achieves the temporal optical outputs by fixing dye laser (DL) frequency. The grating motor of DL1 and DL2 is scanned by computer to form the x-axis (wavelength), and the intensity of the excitation spectrum is the average of ten shots from the gated integrator appearing on the y-axis. The optical signal generated is detected at photomultiplier tubes (PMTs) via confocal lenses (CL), as shown in Fig. S1(g) (See Supplementary materials for detailed experimental setup). While PMT2 is positioned close to the sample to detect hybrid signal (FL + $\boldsymbol{E_{S/AS}}$) with dominant FL emission, PMT1 (near-detector position) and PMT3 (far-detector position) are precisely positioned to detect the generated in-phase spontaneous four-wave mixing (SFWM) (Fig. 1b). By adjusting the GP, one can obtain output signals from different energy levels with different lifetimes. The ratio of FL to $\boldsymbol{E_{S/AS}}$ in a hybrid signal is controlled by GP. Due to the distinct decay rates exhibited by the FL and SFWM, they can be easily differentiated at the PMT by adopting a boxcar GP. Furthermore, Fano resonance strongly depends upon point-group site symmetry of different phases of Eu^{3+} : $BiPO_4$. Fig. 1c shows the proposed model of a non-Hermitian multichannel optical router. Fig. 1d shows the dressing-like Zeeman splitting of $^7F_1$ energy level. For the $^7F_1$ energy level by dressing field quantized rotation, the following splitting energy levels can be obtained: $^7F_{1,\ MJ=-1}$, $^7F_{1,\ MJ=0}$, and $^7F_{1,\ MJ=+1}$.

Theoretical Model for thermal-phonon dressings The proposed model shows that more phonons can couple more energy levels, as shown in Fig. 1a3. The excitations from single laser and two lasers show a single Fano dip (self-dressing) and multi-Fano dips (external dressing), respectively. It is worth mentioning that multidressing can only be generated from photon−phonon multi-Fano interference, not through excitations of one or two lasers. For the Eu^{3+} : $BiPO_4$ sample, unique lattice vibrations can produce phonons with different frequencies which are coupled to different CF splitting levels $^5D_1 \rightarrow {}^7F_1$, $^5D_0 \rightarrow {}^7F_1$, and $^5D_0 \rightarrow {}^7F_3$ in the ion Eu^{3+}. Therefore, more phonon results in effective dressing[36]. The findings in the current work reveal the five sharp dips, which can only be explained by the combined effect of photon dressing and phonon.

The non-Hermitian multi-Fano of one laser By opening field $\boldsymbol{E_1}$, the dressed third-order density matrix element for $\boldsymbol{E_S}$ ($\rho'^{(3)}_S$) and $\boldsymbol{E_{AS}}$ ($\rho'^{(3)}_{AS}$) via perturbation chains $\rho^{(0)}_{00} \xrightarrow{E_1} \rho^{(1)}_{20} \xrightarrow{E_{AS}} \rho^{(2)}_{00} \xrightarrow{E'_1} \rho^{(3)}_{20(S)}$ and $\rho^{(0)}_{00} \xrightarrow{E'_1} \rho^{(1)}_{20} \xrightarrow{E_S} \rho^{(2)}_{00} \xrightarrow{E_1} \rho^{(3)}_{20(AS)}$, respectively, can be written as follows:

$$\rho^{(3)}_{S(2)} = \frac{-iG_1G_{AS}G'_1}{(\Gamma_{20}+i\Delta_1)(\Gamma_{00}+i\Delta_1-i\Delta_{AS}+d_1)(\Gamma_{20}+\Delta_1-i\Delta_{AS}+i\Delta'_1)}$$
$$= \rho'^{(3)}_{S(2)}+\rho'^{(5)}_{S(2)}+\rho'^{(7)}_{S(2)}, \quad (1)$$

$$\rho^{(3)}_{AS(2)} = \frac{-iG_1G_SG'_1}{(\Gamma_{20}+i\Delta'_1 1)(\Gamma_{00}+i\Delta'_1-i\Delta_S+d_2)(\Gamma_{20}+i\Delta'_1 1-i\Delta_S+i\Delta_1)}$$
$$= \rho'^{(3)}_{AS(2)}+\rho'^{(5)}_{AS(2)}+\rho'^{(7)}_{AS(2)}, \quad (2)$$

where, $d_1 = |G_1|^2/(\Gamma_{20}+i\Delta_1-i\Delta_{AS}+d_3)$,

$d_3 = |G_{p1}|^2/(\Gamma_{10}+i\Delta_1-i\Delta_{AS}-i\Delta_{p1})$,

$d_2 = |G_1|^2/(\Gamma_{20}+i\Delta'_1-i\Delta_S+d_4)$,

$d_4 = |G_{p1}|^2/(\Gamma_{10}+i\Delta'_1-i\Delta_S-i\Delta_{p1})$,

$|\rho'^{(3)}_{S/AS}| = (A^2+B^2+C^2+2AB\cos(\Delta\varphi_1)+2AC\cos(\Delta\varphi_2)+2BC\cos(\Delta\varphi_3))^{1/2}$.

The linewidth of the $E_{S/AS}$ signal is $\Gamma_{S/AS} = \Gamma_{20}+\Gamma_{00}+\Gamma_{20}$. The transverse dephase rate $\Gamma_{ij} = (\Gamma_i+\Gamma_j)/2$, where, Γ_{phonon} is related to the sample temperature and $\Gamma_{dressin\ g}$ is associated with dressing. Here, two Fano interferences are controlled by three phases ($\Delta\varphi_1 = \pi$, $\Delta\varphi_2 = \pi$, $\Delta\varphi_3 = 0$). The aforementioned equations show nested double dressing suggesting two-Fano interference is originated from one continuous state $\rho'^{(3)}_{S/AS}$ and two bound states (photon1 $\rho'^{(5)}_{S/AS}$ photon1−phonon1 $\rho'^{(7)}_{S/AS}$). $G_i = -\mu_H H/\hbar$ is the photon Rabi frequency, where, H is the magnetic field for Rabi frequency, μ_H is the magnetic dipole matrix elements levels $|m\rangle$ and $|n\rangle$ and $|m\rangle$ and $|n\rangle$ are the CF-splitting energy levels of $^5D_0$ and $^7F_1$, respectively. Γ_{mn} is the transverse decay rate between levels $|m\rangle$ and $|n\rangle$. The frequency detuning $\Delta_i = \Omega_{mn} - \omega_i$, where, Ω_{kl} is the corresponding atomic transition frequency between levels $|m\rangle$ and $|n\rangle$. ω_i is the frequency of the laser field $\boldsymbol{E_i}$.

Photon excitation is resulted from the interaction of laser light with the host material (Eu^{3+} : $BiPO_4$). On the other hand, phonon excitation arises from the interaction of the doped ion with a source of phonons (crystal lattice vibration), which are vibrations in the crystal lattice. The phonon Rabi frequency is described as the phonon Rabi frequency $G_{pi} = -\mu_{kl}E_{pi}/\hbar$, μ_{kl}, which is the dipole moment between $|k\rangle$ and $|l\rangle$ of CF energy levels in $^7F_1$. ω_{pi} is the phonon frequency of phonon field E_{pi}, which is determined by the vibration frequency of crystal lattice state mode. The Γ_{kl} is the transverse decay rate between $|k\rangle$ and $|l\rangle$. $G_i = -\mu_{kl}E_i/\hbar$ is the frequency detuning, where, Ω_{kl} is the resonant frequency between $|k\rangle$ and $|l\rangle$. ω_i is the frequency of photon field E_i, which is determined by the vibration frequency of crystal lattice state mode. For the three dark states of nested three dressing, the expression (Fig. 5e) can be written as follows:

$$\rho^{(3)}_{S(3)} = \frac{-iG_1G_{AS}G'_1}{(\Gamma_{20}+i\Delta_1+d_{00})(\Gamma_{00}+i\Delta_1-i\Delta_{AS})(\Gamma_{20}+i\Delta_1+i\Delta'_1-i\Delta_{AS}))}$$
$$= \rho'^{(3)}_{S(3)}+\rho'^{(5)}_{S(3)}+\rho'^{(7)}_{S(3)}+\rho'^{(9)}_{S(3)}, \quad (3)$$

$$\rho^{(3)}_{AS(3)} = \frac{-iG_1G_SG'_1}{(\Gamma_{20}+i\Delta'_1+d'_{00})(\Gamma_{00}+i\Delta'_1-i\Delta_S)(\Gamma_{20}+i\Delta'_1+i\Delta_1-i\Delta_S)}$$
$$= \rho'^{(3)}_{AS(3)}+\rho'^{(5)}_{AS(3)}+\rho'^{(7)}_{AS(3)}+\rho'^{(9)}_{AS(3)}, \quad (4)$$

Where, $d_{00} = |G_1|^2/(\Gamma_{20}+i\Delta_1+|G_{p1}|^2/(\Gamma_{10}+i\Delta_1 - i\Delta_{p1}+ |G_{p2}|^2/(\Gamma_{13}+i\Delta_1 - i\Delta_{p1} - i\Delta_{p2})), d'_{00}|G_1|^2/(\Gamma_{20}+i\Delta'_1+|G_{p1}|^2/(\Gamma_{10}+i\Delta'_1 - i\Delta_{p1}+|G_{p2}|^2/(\Gamma_{13}+i\Delta'_1 - i\Delta_{p1} - i\Delta_{p2})))$.

$$\left|\rho'^{(3)}_{S/AS}+\rho'^{(5)}_{S/AS}+\rho'^{(7)}_{S/AS}+\rho'^{(9)}_{S/AS}\right| = (A^2+B^2+C^2+D^2+2AB\cos(\Delta\varphi_1)+ 2AC\cos(\Delta\varphi_2)+2AD\cos(\Delta\varphi_3)+2BC\cos(\Delta\varphi_4)+2BD\cos(\Delta\varphi_5) +2CD\cos(\Delta\varphi_6))^{1/2}$$

Eq. (3)–(4) represent nested three dressing resulting in three-Fano interference, which is originated from an imperfect continuous state ($\rho'^{(3)}_{S/AS}$) and three bound (photon1 $\rho'^{(5)}_{S/AS}$ photon1−phonon1 $\rho'^{(7)}_{S/AS}$ photon1−phonon1−phonon2 $\rho'^{(9)}_{S/AS}$) states. The three Fano interferences are governed by six phases ($\Delta\varphi_1 = \pi, \Delta\varphi_2 = \pi, \Delta\varphi_3 = \pi, \Delta\varphi_4 = 0, \Delta\varphi_5 = 0, \Delta\varphi_6 = 0$). For the four dark states of nested four dressing, the expression can be written as follows

$$\rho^{(3)}_{S(4)} = \frac{-iG_1G_{AS}G'_1}{(\Gamma_{20}+i\Delta_1+d_3)}\frac{1}{(\Gamma_{00}+i\Delta_1 - i\Delta_S)(\Gamma_{20}+i\Delta_1+i\Delta'_1 - i\Delta_S)))}$$

$$= \rho'^{(3)}_{S(4)}+\rho'^{(5)}_{S(4)}+\rho'^{(7)}_{S(4)}+\rho'^{(9)}_{S(4)}+\rho'^{(11)}_{S(4)}, \quad (5)$$

$$\rho^{(3)}_{AS(4)} = \frac{-iG_1G_SG'_1}{(\Gamma_{20}+i\Delta_1+d_4)}\frac{1}{(\Gamma_{00}+i\Delta_1 - i\Delta_S)(\Gamma_{20}+i\Delta_1+i\Delta'_1 - i\Delta_S)))}$$

$$= \rho'^{(3)}_{AS(4)}+\rho'^{(5)}_{AS(4)}+\rho'^{(7)}_{AS(4)}+\rho'^{(9)}_{AS(4)}+\rho'^{(11)}_{AS(4)}. \quad (6)$$

Where, $d_3 = |G_1|^2/\Gamma_{20}+i\Delta_1+|G_{p1}|^2/(\Gamma_{10}+i\Delta_1 - i\Delta_{p1}+ |G_{p2}|^2/(\Gamma_{30}+i\Delta_1 - i\Delta_{p1}+i\Delta_{p2}+|G_{p3}|^2/(\Gamma_{31}+i\Delta_1 - i\Delta_{p1}+i\Delta_{p2} - i\Delta_{p3})))) d_4 = |G_1|^2/\Gamma_{20}+i\Delta'_1+i\Delta_1+|G_{p1}|^2/(\Gamma_{10}+i\Delta'_1+i\Delta_1 - i\Delta_{p1}+|G_{p2}|^2/(\Gamma_{13}+i\Delta'_1+i\Delta_1 - i\Delta_{p1} - i\Delta_{p2}+|G_{p3}|^2/(\Gamma_{03}+i\Delta'_1+i\Delta_1 - i\Delta_{p1} - i\Delta_{p2} - i\Delta_{p3})))))$.

By using Eq. (1) and (2), the interference terms can be written as follows:

$$\left|\rho'^{(3)}_{S/AS}+\rho'^{(5)}_{S/AS}+\rho'^{(7)}_{S/AS}+\rho'^{(9)}_{S/AS}+\rho'^{(11)}_{S/AS}\right| = (A^2+B^2+C^2+D^2+E^2+2AB\cos(\Delta\varphi_1)+2AC\cos(\Delta\varphi_2)+2AD\cos(\Delta\varphi_3)+2AE\cos(\Delta\varphi_4)+ 2BC\cos(\Delta\varphi_5)+2BD\cos(\Delta\varphi_6)+2BE\cos(\Delta\varphi_7)+2CD\cos(\Delta\varphi_8)+2CE\cos(\Delta\varphi_9)+ 2DE\cos(\Delta\varphi_{10})))^{1/2}$$

The dressed third-order density matrix can be approximated as the sum of the third-, fifth-, seventh-, ninth-, and eleventh-order $\boldsymbol{E}_{S/AS}$, governed by dressed SFWM multi-Fano phase $\Delta\varphi_{S/AS} = \varphi^{(L)}_{S/AS} - \varphi^{(K)}_{S/AS}$ ($L < K$). The total phase $\varphi^{(j)}_{S/AS}$ of generated $\boldsymbol{E}_{S/AS}$ is a sum of the initial phase $\varphi^{I(j)}_{S/AS}$, cross-Kerr nonlinear phase $\varphi^{x(j)}_{S/AS}$, and self-Kerr nonlinear phase $\varphi^{s(j)}_{S/AS}$ ($\varphi^{(j)}_{S/AS} = \varphi^{I(j)}_{S/AS}+\varphi^{s(j)}_{S/AS}+\varphi^{x(j)}_{S/AS}$). Therefore, multi-Fano interference could be constructive or destructive depending upon the total phase when the condition is set as $\Delta\varphi_{S/AS} = 0$ ($i = 1$ to 10), which results in 10 bright states. However, at 0 or π ($i = 1$ to 10), the result shows 10 dark states. For the four dark states, the expression can be written as $|\rho'^{(3)}_{S/AS} - \rho'^{(5)}_{S/AS} - \rho'^{(7)}_{S/AS} - \rho'^{(9)}_{S/AS} - \rho'^{(11)}_{S/AS}|$. The four-Fano is controlled by ten phases ($\Delta\varphi_1 = \pi, \Delta\varphi_2 = \pi, \Delta\varphi_3 = \pi, \Delta\varphi_4 = \pi, \Delta\varphi_5 = 0, \Delta\varphi_6 = 0, \Delta\varphi_7 = 0, \Delta\varphi_8 = 0, \Delta\varphi_9 = 0, \Delta\varphi_{10} = 0$)). Eq. (1) and (2) show four-Fano interference, which is originated from an approximate continuous state $\rho'^{(3)}_{S/AS}$, photon1 $\rho'^{(5)}_{S/AS}$, photon1−phonon1 $\rho'^{(7)}_{S/AS}$, photon1−phonon1−phonon2 $\rho'^{(9)}_{S/AS}$, photon1−phonon1−phonon2−phonon3 $\rho'^{(11)}_{S/AS}$ states. Moreover, the SFWM multi-Fano interference between continuous and multibound states is very obvious when the Δ_1 is scanned.

The non-Hermitian multi-Fano of two lasers In a Λ-type three-level system, third-order $\rho^{(3)}_{S/AS}$ via $\rho^{(0)}_{00} \xrightarrow{E_1} \rho^{(1)}_{20} \xrightarrow{E_{AS}} \rho^{(2)}_{00} \xrightarrow{E'_1} \rho^{(3)}_{20(S)}$ and $\rho^{(0)}_{00} \xrightarrow{E'_1} \rho^{(1)}_{20} \xrightarrow{E_S} \rho^{(2)}_{00} \xrightarrow{E_1} \rho^{(3)}_{20(AS)}$, respectively, can be written as follows:

$$\rho^{x(3)}_{S(3)} = \frac{-iG_1G_{AS}G'_1}{(\Gamma_{20}+i\Delta_1+d_5)}\frac{1}{(\Gamma_{00}+i\Delta_1 - i\Delta_{AS})(\Gamma_{20}+i\Delta_1+i\Delta'_1 - i\Delta_{AS})))}$$

$$= \rho'^{x(3)}_{S(3)}+\rho'^{x(5)}_{S(3)}+\rho'^{x(7)}_{S(3)}+\rho'^{x(9)}_{S(3)}, \quad (7)$$

$$\rho^{x(3)}_{AS(3)} = \frac{-iG_1G_SG'_1}{(\Gamma_{20}+i\Delta_1+d_6)}\frac{1}{(\Gamma_{00}+i\Delta_1 - i\Delta_S)(\Gamma_{20}+i\Delta_1+i\Delta'_1 - i\Delta_S)))}$$

$$= \rho'^{x(3)}_{AS(3)}+\rho'^{x(5)}_{AS(3)}+\rho'^{x(7)}_{AS(3)}+\rho'^{x(9)}_{AS(3)}. \quad (8)$$

where, $d_5 = |G_2|^2/(\Gamma_{20}+i\Delta_1+i\Delta_2+|G_{p1}|^2/(\Gamma_{10}+i\Delta_1+i\Delta_2 - i\Delta_{p1} +|G_{p2}|^2/(\Gamma_{13}+i\Delta_1+i\Delta_2 - i\Delta_{p1} - i\Delta_{p2})))d_6 = |G_2|^2/(\Gamma_{20}+i\Delta'_1+ i\Delta_2+|G_{p1}|^2/(\Gamma_{10}+i\Delta'_1+i\Delta_2 - i\Delta_{p1}+|G_{p2}|^2/(\Gamma_{13}+i\Delta'_1+i\Delta_2 - i\Delta_{p1} -i\Delta_{p2})))$.

The equations represent three-Fano interference, which is originated from the photon1−photon2 continuum state $\rho''^{x(3)}_{S/AS}$ and three bound states (photon1 $\rho''^{(5)}_{S/AS}$, photon1−phononon1 $\rho''^{(7)}_{S/AS}$, and photon1−phonon1−phonon2 $\rho''^{(9)}_{S/AS}$). Three-Fano has six phases ($\Delta\varphi_1 = \pi, \Delta\varphi_2 = \pi, \Delta\varphi_3 = \pi\Delta\varphi_4 = 0, \Delta\varphi_5 = 0, \Delta\varphi_6 = 0$). The interference between continuous and multibound states of SFWM multi-Fano appears when the Δ_2 is scanned.

Through the Eu^{3+} : $BiPO_4$ crystal lattice vibrations, the phonon dressing can control multi-Fano interference. Fig. 2a shows the spectral evolution of hybrid signal (FL + SFWM) from single Fano to triple Fano obtained from the (0.5 : 1) Eu^{3+} : $BiPO_4$ sample by changing GP (5 μs, 500 μs, 1 ms) when $\boldsymbol{E_1}$ is scanned at 300 K. The (0.5 : 1) Eu^{3+} : $BiPO_4$ crystal exhibits three distinct fine-structure energy levels named as $^5D_1 \rightarrow {}^7F_1$ (magnetic dipole transition), $^5D_0 \rightarrow {}^7F_1$ (magnetic dipole transition), and $^5D_0 \rightarrow {}^7F_3$ (induced electric dipole transition) at the CF of about 10^6 V/cm. The spectral signal recorded at PMT1 (Fig. 2a11) shows three Fano interference resulting from the coexistence of dressing and fine-structure energy levels splitting ($^5D_0 \rightarrow {}^7F_1$ in Fig. 5g1), whereas three Fano dips (three dark states) come from destructive

interference between approximate continuous state ($\rho'^{(3)}_{AS(3)}$) and three bound states ($\rho'^{(5)}_{AS(3)}$, $\rho'^{(7)}_{AS(3)}$, $\rho'^{(9)}_{AS(3)}$) are controlled by Fano phases ($\Delta\varphi_1 = \pi$, $\Delta\varphi_2 = \pi$, and $\Delta\varphi_3 = \pi$) modeled through Eq. (3) and (4). It is noteworthy that the magnitudes of the two Fano peaks are greater than those of the three Fano dips because of more pronounced splitting of energy levels within the $^7F_1$ state than the nested three dressing. $|G_1|^2/(\Gamma_{20}+i\Delta_1+|G_{p1}|^2/(\Gamma_{10}+i\Delta_1 - i\Delta_{p1}+|G_{p2}|^2/(\Gamma_{13}+i\Delta_1 - i\Delta_{p1} - i\Delta_{p2})))$ from Eq. (3) and (4). The validation of this is supported by our theoretical findings as illustrated in Fig.2 h3 at $\Delta_1 = -50$. When the GP approaches 1 ms, the three suppression Fano dips (Fig. 2a31) tends to be more prominent than the enhancement Fano peaks. This observation can be attributed to the dominance of nested three dressing in the completion between the splitting and dressing of the energy levels. In Fig. 2a21, the first Fano dip is stronger than the third Fano dip, which can be attributed to the greater influence of the linear polarization dipole moment in energy level $^7F_1$, $MJ = 0$ than that of the circular partial dipole moment in the energy level (μ_L μ_C). The theoretical results (Fig. 2g and h) validate the multi-Fano evolution (Fig. 2a). In Fig. 2a12, two Fano interference is resulted from the coexistence of double dressing and energy levels' splitting ($^5D_0 \rightarrow {}^7F_1$), where two Fano dips come from interference in an approximate continuous state $\rho'^{(3)}_{S(2)}$ and two bound states $\rho'^{(5)}_{S(2)}$, $\rho'^{(7)}_{S(2)}$ controlled by Fano phase ($\Delta\varphi_1 = \pi$, $\Delta\varphi_2 = \pi$). The practical results obtained align precisely with the theoretical results depicted in Fig. 2h2 (simulated at $\Delta_1 = -50$). When the GP is increased to 500 μs (Fig. 2a22), the two Fano dips evolve into three Fano dips due to sensitive phonon dressing ($|G_{p1}|^2$, $|G_{p2}|^2$) and easy distinction for in-phase SFWM. When GP is at 1 ms (Fig. 2a23), the right first Fano dip is the strongest due to more dressing interaction of $^7F_{1,\,MJ=0}$ and $^7F_{1,\,MJ=+1}$. The single Fano interference (Fig. 2a13) occurs due to the coexistence of single dressing and energy level splitting. In contrast, a single Fano dip emerges from the interference between dark states and bright states, a phenomenon regulated by the Fano phase ($\Delta\varphi = \pi$) and modeled by $\rho'^{(3)}_{AS(1)}+\rho'^{(5)}_{AS(1)}$. When GP is increased to 1 ms, two Fano peaks are changed into single Fano dip due to photon dressing ($|G_1|^2$) dominance.

The spectral evolution of two sharp peaks to five Fano interference, recorded at PMT2 by adjusting GP, is displayed in Fig. 2b. The two sharp peaks observed in Fig. 2b11–2b13 can be attributed to the splitting of energy levels during the transitions $^5D_1 \rightarrow {}^7F_1$, $^5D_0 \rightarrow {}^7F_1$, and $^5D_1 \rightarrow {}^7F_3$, respectively. Multi-Fano interference seen at PMT2 (Fig. 2b) is stronger than that at PMT1 (Fig. 2a) due to the strong SFWM at the near detector. The spectral evolution observed at PMT3 (Fig. 2c) exhibits behavior that is identical to that observed at PMT1. The Fano interference in Fig. 2d–f, resulting from the interaction of two lasers, is stronger than that of a single laser (Fig. 2a–c), which is mostly ascribed to two lasers dressing enhancement. However, the left first Fano dip is stronger than the left third Fano dip in Fig. 2d, f, which is mainly attributed to more dressing interaction effect between $^7F_{1,\,MJ=+1}$ and $^7F_{1,\,MJ=0}$.

Fig. 3a shows the spectral evolution of multi-Fano interference from three Fano dips to a single Fano dip in the (7 : 1) Eu^{3+} : $BiPO_4$ crystal corresponding to Fig. 3c when $\boldsymbol{E_1}$ is scanned. In Fig. 3a11, two Fano peaks and three Fano dips come from nested three dressing $\left(|G_1|^2/\Gamma_{20}+i\Delta_1+|G_{p1}|^2/(\Gamma_{10}+i\Delta_1 - i\Delta_{p1}+|G_{p2}|^2/(\Gamma_{30}+i\Delta_1 - i\Delta_{p1}+i\Delta_{p2})\right)$ and can be controlled through the Fano phase ($\Delta\varphi_1 = \pi$, $\Delta\varphi_2 = \pi$, $\Delta\varphi_3 = \pi$), corresponding to the simulation in Fig. 2g3. The Hamiltonian ($H = i\hbar\kappa_1\alpha_1^\dagger\alpha_{p1}^\dagger\alpha_{p2}^\dagger$ where $\kappa_1 = -i\varpi\chi_1^{(9)}E_S E_{p1}E_{p2}E_1^3/2$) shows strong dressing coupling between photon1 ($\alpha_1^\dagger$), sample phonon1 ($\alpha_{p1}^\dagger$), and sample phonon2 ($\alpha_{p2}^\dagger$). The energy level splitting ($^5D_0$–$^7F_3$) and dressing coexistence lead to two Fano interferences in Fig. 3a12, where, two Fano dips can be explained by nested two dressing ($|G_1|^2/\Gamma_{20}+i\Delta_1+|G_{p1}|^2/(\Gamma_{10}+i\Delta_1 - i\Delta_{p1})$) controlled by Fano phase

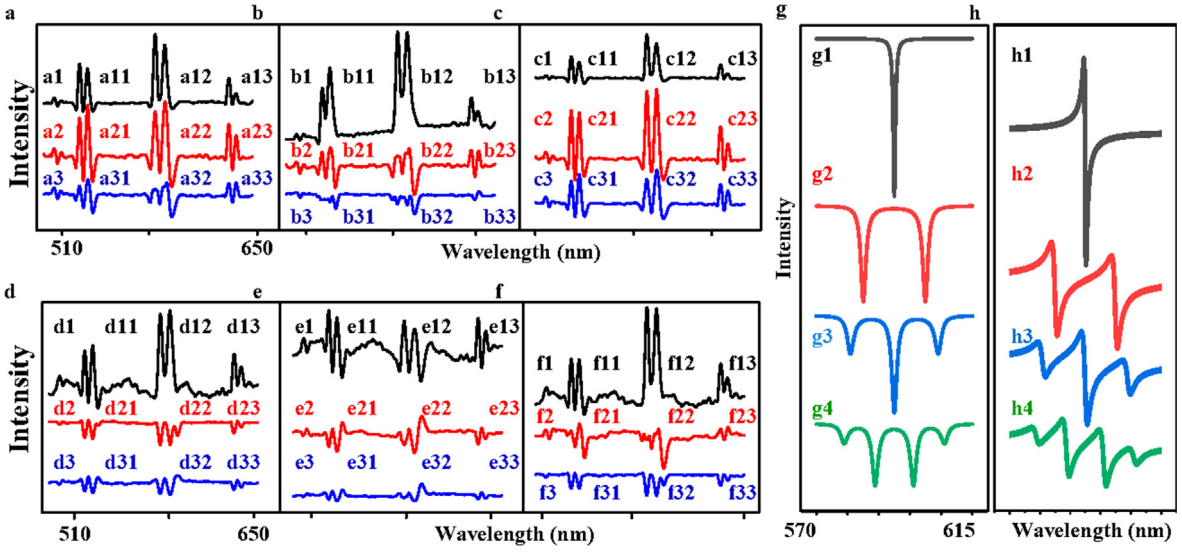

Fig. 2 | Spectral intensity signal measured from the Eu^{3+} : $BiPO_4$ crystal with molar ratio (0.5 : 1) by scanning E_1; **a,** PMT1; **b,** PMT2 and **c,** PMT3. a1–a3, the spectral signal intensity measured at different gate positions (5 μs, 500 μs, and 1 ms). b1–b3 and c1–c3 are the same GP as a1-a3. **d**, **e,** and **f,** Spectral intensity from (0.5 : 1) Eu^{3+} : $BiPO_4$ measured at PMT1, PMT2, and PMT3, respectively, when $\boldsymbol{E_1}$ is scanned while $\boldsymbol{E_2}$ is fixed at 588 nm (laser power = 7 mW, temperature = 300 k, gate width = 200 ns). **g** and **h,** Theoretical results for dressing evolution corresponding to **2a** at $\Delta_1 = 0$ and corresponding **3a** at $\Delta_1 = -50$, respectively. Abbreviations: GP, gate position; PMT, photomultiplier tube.

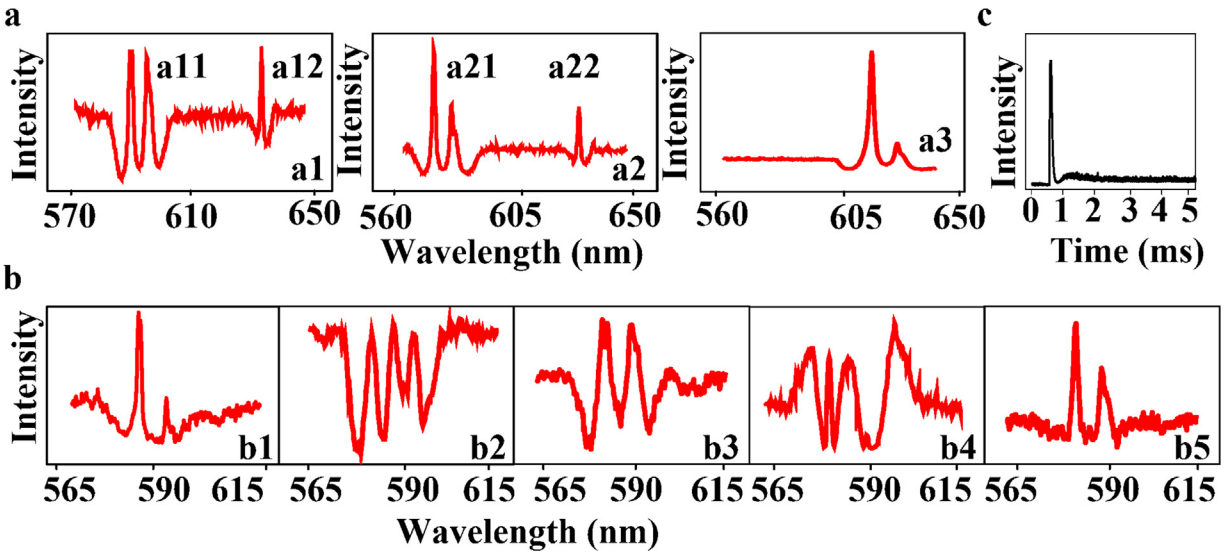

Fig. 3 | Measured spectral intensity of the hybrid signal from (7 : 1) phase Eu $^{3+}$: BiPO $_4$ at PMT1 by fixing GP (30 μs), gate width (500 ns), and temperature (300 K). a, Different laser excitation. a1, Scan $\boldsymbol{E}_2$ only; a2, Scan $\boldsymbol{E}_1$ while $\boldsymbol{E}_2$ is fixed at 588 nm; a3, scan $\boldsymbol{E}_2$ only. b1–b5, Measured spectral from (0.5 : 1) Eu^{3+} : $BiPO_4$ at PMT2 and 9 mW power. **b,** GP (500 μs), and gate width (200 ns). b1, Scanning $\boldsymbol{E}_1$ while fixing $\boldsymbol{E}_2$ (588 nm) and low temperature (77K); b2, scanning $\boldsymbol{E}_1$ only at 300 K; b3, Scan $\boldsymbol{E}_1$ is scanned while $\boldsymbol{E}_2$ is fixed at 588 nm at room temperature (300 K); b4, Scan $\boldsymbol{E}_1$ is scanned and $\boldsymbol{E}_2$ (588 nm), GP (500 μs), gate width (15 μs), and 300 K temperature; b5, scanning $\boldsymbol{E}_1$ at GP (1 ms), gate width (200 ns) and 300 K temperature. Abbreviations: PMT, photomultiplier tube; GP, gate position. **c**, Show the measured time-domain signal from Eu^{3+}:$BiPO_4$.

($\Delta\varphi_1 = \pi, \Delta\varphi_2 = \pi$) mentioned in Eq. (1) and (2). The amplitude of three Fano dips (Fig. 3a11) is reduced as a consequence of the weak dressing resulting from the interaction of two lasers, when compared to Fano dips illustrated in Fig. 3a11. Similarly, the two Fano interference tends to be weak in Fig. 3a22, which aligns with the simulation results depicted in Fig. 2g2. When compared to the Fano interference in Fig. 3a11, the Fano interference seen in Fig. 3a3 is weak. This difference can be attributed to the influence of a narrower excitation band, which controls the extent of crystal vibration phonons in the system.

In Fig. 3b1, two sharp peaks are resulted from competition between energy level splitting ($^5D_0$–$^7F_1$) dominance and dressing, which can be further explained by two lasers interaction and low-intensity phonon dressing ($|G_{p1}|^2$, $|G_{p2}|^2$) at low temperatures. Moreover, the spectral linewidth of the peak is sharp (Fig. 3b1). The four Fano dips (Fig. 3b2) come from destructive interference $\rho'^{(3)}_{S/AS}+\rho'^{(5)}_{S/AS}+\rho'^{(7)}_{S/AS}+\rho'^{(9)}_{S/AS}+\rho'^{(11)}_{S/AS}$ from Eq. (5) and (6). The control of Fano dips and peaks can be achieved by manipulating the Fano phase, where the dips are attributed to the presence of four dark states that are observed at $\Delta\varphi_1 = \Delta\varphi_2 = \Delta\varphi_3 = \Delta\varphi_4 = \pi$. Such four dressing dips come from photon1 dressing $|G_1|^2$ and three phonons dressing ($|G_{p1}|^2$, $|G_{p2}|^2$, $|G_{p3}|^2$) with Hamiltonian $H = i\hbar\kappa_1\alpha_1^\dagger\alpha_{p1}^\dagger\alpha_{p2}^\dagger\alpha_{p3}^\dagger + H.c.$, where, $\kappa_1 = -i\varpi\chi_1^{(11)}E_{AS}E_S E_{p1}E_1^3 E_{p2} E_{p3}/2$.It shows the strong dressing coupling among photon1 ($G_1^\dagger$)–phonon1 ($G_{p1}^\dagger$)–phonon2 ($G_{p2}^\dagger$)–phonon3 ($G_{p3}^\dagger$). In Fig. 3b2, broad profile linewidth is caused by three phonons dressing in (0.5 : 1) $BiPO_4$. The Fano phase for four dark states and six bright states can be written as $\Delta\varphi_1 = \Delta\varphi_2 = \Delta\varphi_3 = \Delta\varphi_4 = \pi$ and $\Delta\varphi_5 = \Delta\varphi_6 = \Delta\varphi_7 = \Delta\varphi_8 = \Delta\varphi_9 = \Delta\varphi_{10} = 0$, respectively. The presence of six bright states surpasses the number of four dark states due to the additional bright state being integrated into the existing five bright states. The left first Fano dip is stronger than the left fourth Fano dip in Fig. 3b2 due to $\mu_C > \mu_L$. These results coincide with our theoretical results obtained for nested four dressing at $\Delta_1 = 50$.

In Fig. 3b3, the signal observed by scanning $\boldsymbol{E_1}$ while fixing $\boldsymbol{E_2}$ (588 nm) shows multi-Fano interference with three Fano dips resulting from nested three dressings ($|G_2|^2/(\Gamma_{20}+i\Delta_2+|G_{p1}|^2/(\Gamma_{10}+i\Delta_2 - i\Delta_{p1})+|G_{p2}|^2/(\Gamma_{30}+i\Delta_2 - i\Delta_{p1}+i\Delta_{p2}))$) in Eq. (7) and (8) and four Fano peaks from energy level splitting and Autler–Townes (AT) splitting. In addition, it is observed that single-laser excitation (Fig. 3b2) exhibits a greater number of dressing dips than two lasers excitation (Fig. 3b3). This can be attributed to the interaction between the two lasers within the crystal, which reduces the dressing effect, as illustrated in Fig. 2e. The observed outcome is consistent with the findings obtained from the nested three-dressing simulation at $\Delta_1 = 50$. The spectral signal depicted in Fig. 3b4 exhibits strong three Fano interference at 15 μs gate width for the (0.5 : 1) Eu^{3+} : $BiPO_4$ sample mostly attributed to the dominance of SFWM dominance. The three multi-Fano dips can be explained by photon2 and two phonons nested dressing ($|G_2|^2$, $|G_{p1}|^2$, $|G_{p2}|^2$). By comparing the Fano dips observed in Fig. 3b3 to those in Fig. 3b4, it is evident that the latter exhibits three consecutive Fano dips. This can be attributed to a more phonon dressing. As gate width increases from 200 μs (Fig. 3b3) to 500 ns (Fig. 3b4), the increasing ratio of SFWM in hybrid signal leads to high spectral resolution. The bright and dark states can be controlled by adjusting the phase between zero and π. As the gate width expands, the number of bright states rises, as illustrated in Fig. 3b4. The three Fano dips and four Fano peaks are originated from the two-laser excitation with a Fano phase of three dark states ($\Delta\varphi_1 = \Delta\varphi_2 = \Delta\varphi_3 = \pi$) and three bright states ($\Delta\varphi_4 = \Delta\varphi_5 = \Delta\varphi_6 = 0$), respectively. The additional peak is originated from pure constructive states at Fano phases $\Delta\varphi_i = 0$ (i = 1, 2, 3, 4, 5, 6). When the GP reaches to 1 ms, Fig. 3b5 depicts clearly defined sharp peaks that can be attributed to the dominance of CF splitting, as illustrated in Fig. 1a2. Based on the findings obtained from our research, it can be concluded that the (0.5 : 1) H-phase Eu^{3+} : $BiPO_4$ exhibits strong dressing Fano interference

compared to (7 : 1) M-phase Eu^{3+} : $BiPO_4$ resulting from more phonon dressing.

Figs. 4a and b discuss the evolution of SFWM from FL in a hybrid signal for (6 : 1) and (1 : 1) Eu^{3+} : $BiPO_4$, respectively. At near GP, the dressing effect is weak, leading to a spectral peak characterized by low resolution and a broad linewidth, as shown in Fig. 4a1. Upon increasing the GP (20 μs), an emergence of three Fano dips and two Fano peaks is apparent, (Fig. 4a2), resembling the pattern depicted in Fig. 2a22. The observed phenomenon can be attributed to the reduced impact of dressing detuning, resulting in a decreased photon dressing effect and high SFWM resolution. By further increasing GP (200 μs), the three Fano dips tend to be stronger in Fig. 4a3 due to one-photon dressing ($|G_1|^2$) and two-phonon dressings ($|G_{p1}|^2$, $|G_{p2}|^2$) as modeled from Eq. (3) and (4). As the GP reaches 500 μs, the five Fano-dips in Fig. 4a4 are originated from energy levels $^7F_1$ symmetrical splitting of one laser excitation.

Fig. 4b shows the evolution from a single broad dip to sharp multi-dips for (1 : 1) Eu^{3+} : $BiPO_4$ under the same experimental conditions as described in Fig. 4a. In comparison to Fig. 4a1, the broad dip is shown in Fig. 4b1 due to higher frequency (w_{pi}) phonon for (1 : 1) than (6 : 1) Eu^{3+} : $BiPO_4$, which results in strong phase transition phonon dressing ($|G_{pi}|^2/(i\Omega_{mn} - iw_{pi})$) with $\Delta_1 - \Delta_{p1}$, $\Delta_1 - \Delta_{p1}+\Delta_{p2}$, $\Delta_1 - \Delta_{p1}+\Delta_{p2} - \Delta_{p3}$, which is close to resonance compared to the (6 : 1) sample, as shown in Fig. 4a. As GP reaches 500 μs, the five Fano dips are shown in Fig. 4b4. So, the phase transition phonon dressing is stronger in the (1 : 1) sample than that in the (6 : 1) sample. In summary, in contrast to the FL signal, the SFWM signal exhibits higher resolution. The presence of multiple Fano dips can be readily observed in the signal generated by SFWM.

From our results, we have realized the wavelength division multiplexing of both classical and coherent channels. The non-classical SFWM may be effectively multiplexed with divided Fano dip across a range of 1 μs to 500 μs. This multiplexing technique enables the routing of identical information across many channels, ranging from one channel (Fig. 4b1) to five channels (Fig. 4b4). A non-Hermitian multichannel router can be realized by non-Hermitian control real-part quantization (Fig. 1c), and the routing process can be achieved by changing the boxcar GP. Similarly, when GP is at 500 μs, the coherent channel output can be multiplexed to five divided Fano dips for routing the same information to different channels. Fig. 4b shows two adjacent dips with relative distance between many dips. Such a phenomenon (pure dip to five Fano dip) is analogous to routing. Such results are used for routing. Here we adopt channel equalization ratio ($P = 1 - \sqrt{\sum_1^{N-1}(s_i - a)^2/a}$) to measure demultiplexing, where a is the area of one dip and s_i is the area of each dip or gap between dips. When $s_i \approx a$,

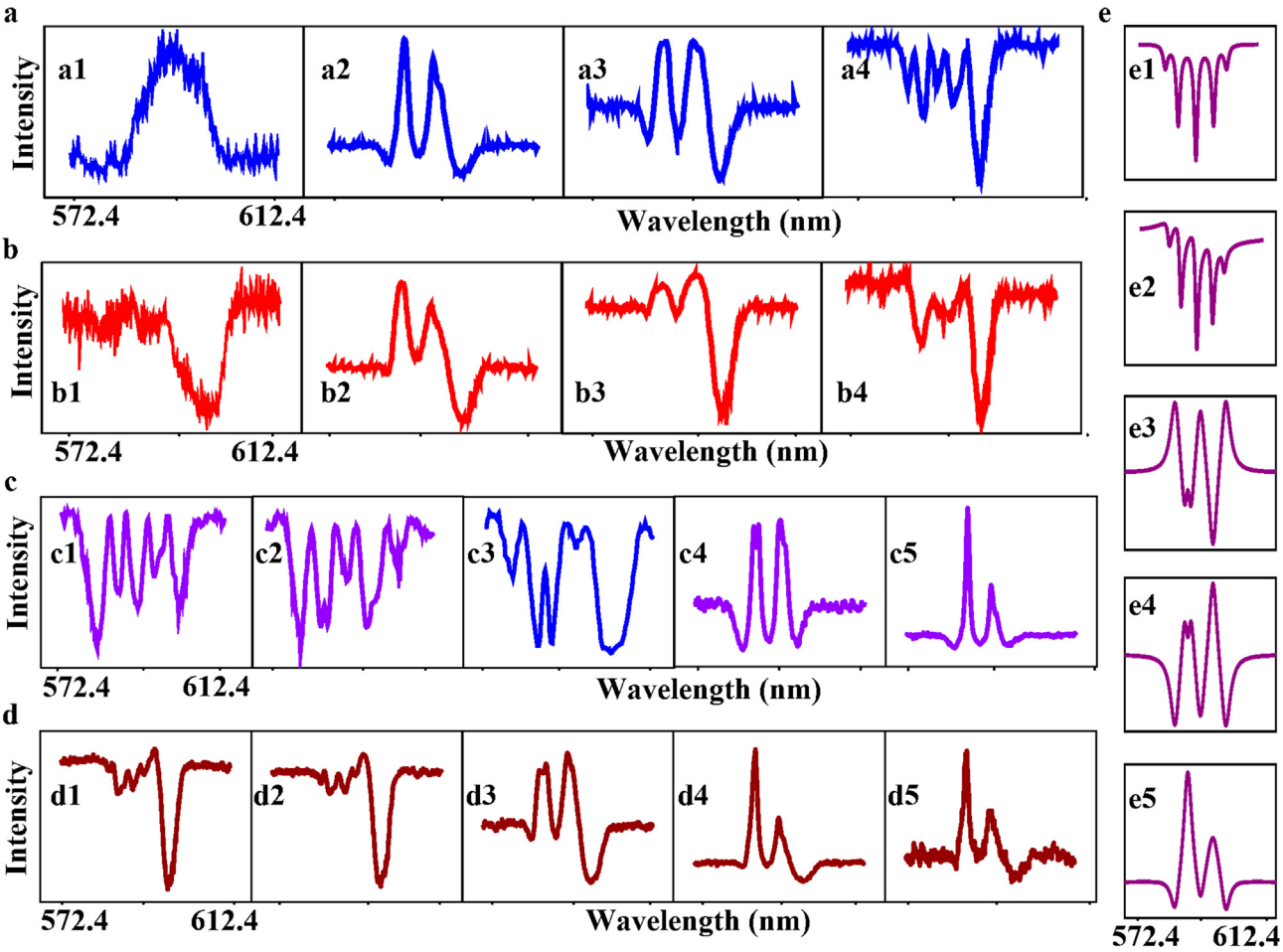

Fig. 4 | Measured spectral signal for different samples. **a, b,** Spectral intensity of hybrid signal measured at PMT1 from (6 : 1) and (1 : 1) Eu^{3+} : $BiPO_4$ crystals, respectively, by scanning Δ_1 with gate position being 1 μs, 20 μs, 200 μs, and 500 μs. **c, d,** Spectral intensity of (0.5 : 1) and (1 : 1) Eu^{3+} : $BiPO_4$ crystal versus Δ_1 by increasing power of $\boldsymbol{E_1}$ from 9 mW to 1 mW, respectively. **e,** Theoretical results corresponding to **c**. Abbreviation: PMT, photomultiplier tube.

DOI: 10.1016/j.chip.2023.100077

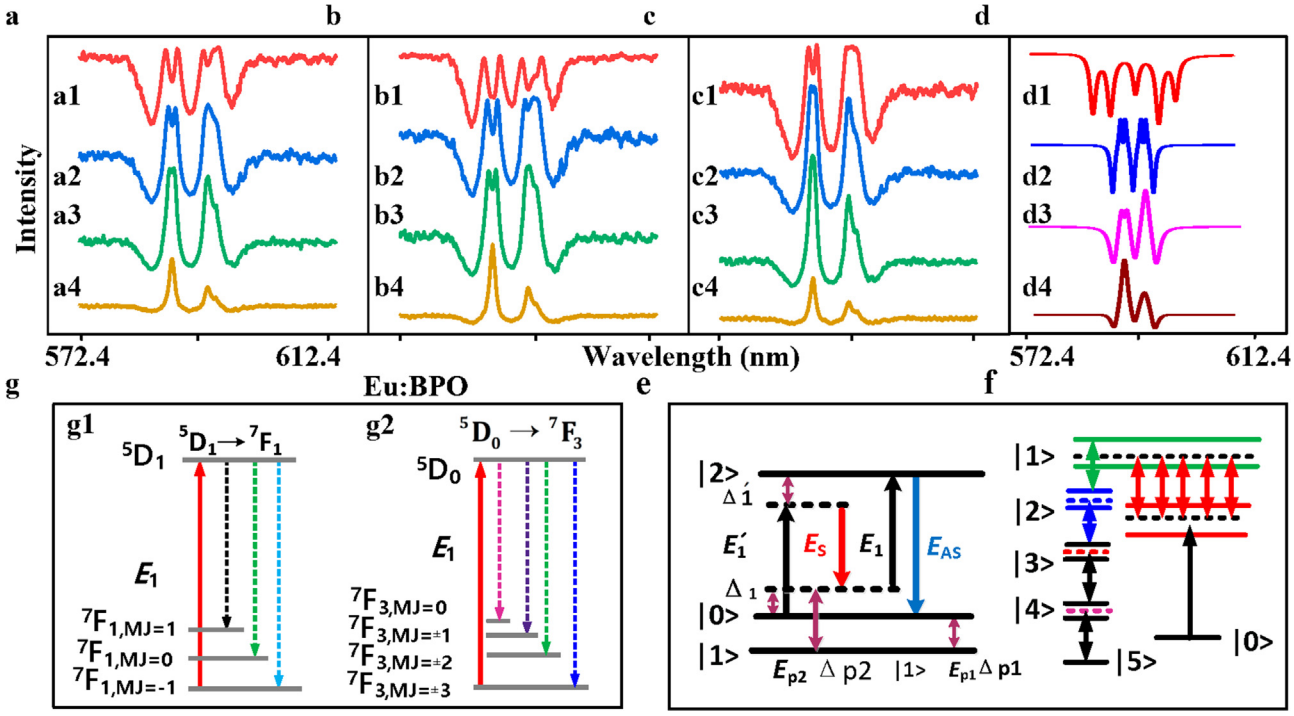

Fig. 5 | Different spectral signals at different powers. a–c, Spectral intensity of the hybrid signal from the (0.5 : 1) Eu^{3+} : $BiPO_4$ plotted versus Δ_1 by increasing $\boldsymbol{E_1}$ power measured at PMT1, PMT2, and PMT3, respectively, at a fixed gate width (200 ns), gate position (500 μs) and temperature (300 K). **d,** Theoretical results by scanning Δ_2 from −50 to 50 and by fixing Δ_1 at −500, −250, 0, 250 to 500. **e,** SFWM dressing energy level. **f,** Five nested dressing energy levels. **g,** Fine structure energy-level diagram of Eu^{3+} : $BiPO_4$ for transition $^7F_1 \rightarrow {}^5D_1$ and $^7F_3 \rightarrow {}^5D_0$, respectively. Abbreviation: PMT, photomultiplier tube.

P is maximum (100%), more balanced and stable spatial channels were obtained. From Fig. 4b, the channel equalization ratio *P* has the potential to reach values ranging from 60% to 80%.

Fig. 4c and d represent the spectrum evolution from multi-Fano interference to two sharp peaks for (0.5 : 1, 1 : 1) $BiPO_4$, respectively, versus changing power. In Fig. 4c, the spectral intensity for the (0.5 : 1) Eu^{3+} : BiPO4 sample is shown at the near detector (PMT2). The laser power was changed from 9 mW to 1 mW at 300 K. When the power is high, strong $|G_1|^2$ results in five dressing dips (Fig. 4c1, 4c2) from $^7F_1$ symmetrical splitting (similar to Fig. 4a4), which is corresponding to the simulation result at $\Delta_1 = 0$ in Fig. 4e1–e4, respectively. Also, the left first to third Fano dip for energy level $^7F_{1,\ MJ=\pm1}$ as shown in Fig. 4c1–c2, come from nested three dressings, where the left fourth to fifth Fano dips come for energy level $^7F_{1,\ MJ=\pm1}$ as shown in Fig. 4c1–c2, owing to nested double dressing. Fig. 4d shows the spectral intensity for the (1 : 1) Eu^{3+} : $BiPO_4$ at PMT2 by changing power (9 mW, 7 mW, 5 mW, 3 mW, 1 mW). When the power of $\boldsymbol{E_1}$ is decreased to 1 mW, the two sharp peaks are observed, as shown in Figs. 4c5 and d5, due to weak dressing ($|G_1|^2 \approx 0$) at low power.

The nested dressing multi-Fano dips observed in our studies can be associated with third-order quantization, as depicted in Fig. 1d. Herein, EP or non-Hermitian control originating from real and imaginary quantization alignment is discussed, as shown in Fig. 1d. The non-Hermitian EP manifests itself via CF splitting independently of any dressing effects. Fig. 4a–d exhibit full- and half-EP control, respectively. The multi-Fano real-part quantization channels can be defined as $N = N_m/N_{EP}$, where N_m represents the number of dressing dips in SFWM signal, and N_{EP} is the number of peaks at EP control (two CF peaks), where, each peak represents one level ($^7F_{1,\ MJ=\pm1}$, or $^7F_{1,\ MJ=0}$). The SFWM multi-Fano quantization leads to different channels (N = 3 (fourth-order) at $^7F_1$, $^7F_{1,\ MJ=\pm1}$ for the left EP peak (Fig. 4a4–a2 and N = 2 (third-order) at $^7F_{1,\ MJ=0}$ for the right EP peak (Fig. 4c5–c1). Similarly, N = 1 (second-order) at $^7F_{1,\ MJ=0}$, and third-order N = 2 at $^7F_{1,\ MJ=\pm1}$ exhibited from each level in Fig. 4b and N = 2 (third-order) exhibited in each level from Fig. 4d.

Fig. 5 shows the evolution from multiple dips to two peaks when the laser of $\boldsymbol{E_1}$ is kept high. Fig. 5a and b show five Fano dips resulting from five nested dressings (three dressing in $^7F_{1,\ MJ=\pm1}$ and two dressing in $^7F_{1,\ MJ=0}$) in a manner similar to that described in Fig. 4c1. When the laser power is lowered, there is a reduction in photon dressing, which leads to the diminishing of three Fano dips resulting from three distinct fine structure energy levels ($^7F_{1,\ MJ=-1}$, $^7F_{1,\ MJ=0}$, $^7F_{1,\ MJ=1}$). This reduction in photon dressing also contributes to the decrease in phenomenon illustrated in Fig. 4c4. When the power reaches 1 mW, only two sharp peaks appear as shown in Fig. 5a4–c4 due to weak photon dressing. From Fig. 5a1–a4, it can be seen that the center of the peak remains unchanged due to strong phonon dressing. When comparing the signal measurements of PMT2 with PMT1 and PMT3, it is observed that the signal measured at PMT2 exhibits a stronger dressing effect. This can be attributed to its proximity to the sample, allowing it to detect FL with a higher amplitude, resulting in a more significant dressing dip. Theoretical results are displayed in Fig. 5d in accordance with experimental results (Fig. 5b).

Owing to the earlier explanations, Fig. 5 shows similar EP control for SFWM multi-Fano quantization (half-EP control). Fig. 5b1 shows channel N = 3 (fourth-order) at $^7F_{1,\ MJ=\pm1}$ for the left EP peak b4 and exhibits N = 2 (third-order) at $^7F_{1,\ MJ=0}$ in b1 for the right EP peak Fig. 5b4. Similar results were observed for Fig. 5a, c.

Fig. 6a shows the EP evolution vs the ratio (G_{p1}/Γ_{20}) between photon−phonon dressing Rabi frequency and transverse dephase rate between level |2> and |0>. The theoretical results are corresponding to nested double dressing. At $G_{p1}/\Gamma_{20} = 0.5$, one energy level splits into a real part and an imaginary part. At internal dressing $G_1/\Gamma_{20} = 0.5$, the real and imaginary parts are split as shown in Fig. 6a3, a4, respectively. The splitting of the real part and the imaginary part of the nested double dressing does not occur simultaneously. When the third-order splitting (G_1/Γ_{20}) occurs in the real part (Fig. 6a3), the corresponding imaginary part (Fig. 6a4) will have the second-order splitting (G_{p1}/Γ_{20}). Thus, the real-part splitting is larger than the imaginary part splitting. The imaginary part is nonlocal, more degenerate and non-Abelian, and highly symmetric. The real part is local, less degenerate and Abelian, and low symmetric. More importantly, the real part is changed from local, Abelian, and more degenerate to nonlocal, non-Abelian, and less degenerate in third-order systems. The dominance of real-part splitting ($G > \Gamma$) shows high-order router; however, the dominance of imaginary part splitting ($\Gamma > G$) shows low-order router. The non-Hermitian EP is a point without dressing. Such an EP can be achieved by varying various external parameters. Such an EP can be achieved by changing different external parameters. The GP is the primary parameter. When the GP is changed from middle (hybrid) to far (SFWM), there exists the EP between hybrid and SFWM. For the nested double dressing, the dressing term is already solved, and it is converted into a univariate cubic equation to be solved, so three eigenvalues are obtained, but in our model, the photon-dressing-like Zeeman splits three energy levels, as shown in Fig. 1a4. The $^7F_{1,\,MJ\,=\,-1}$ and $^7F_{1,\,MJ\,=\,+1}$ energy levels are dressed by two phonons (phonon1 and phonon2) and the other two phonons (phonon3 and phonon4), respectively. However, the $^7F_{1,\,MJ\,=\,0}$ energy level is dressed by one photon (photon1). So, eight eigenvalues can be obtained by solving the equations of two nested double dressings and one single dressing. Moreover, the experimental results are a subset of the theoretical simulation.

Figs. 6c and d show the spectral intensity signal obtained from (0.5 : 1) Eu^{3+} : $BiPO_4$ (C_2 symmetry) and H-phase Eu^{3+} : $NaYF_4$ (Cs symmetry), respectively. In this experiment, the competition between real a and imaginary ib eigenvalues based on nested photon−phonon dressing is discussed. The detailed model of EPs' control based on different laser dressings is depicted in Tables S1-S4 (Supplementary materials). It is worthy to be mentioned that the GP affects the dephase rate (Γ) at the spectral signal. In other words, the ratio of G and Γ can be tuned by changing the GP. In Fig. 4c, Fig. 5b1, and Fig. 6c1, the visible five Fano dips can be observed due to the dominance of the nested dressing ($|G_1|^2$, $|G_{p1}|^2$, $|G_{p2}|^2$, $|G_{p3}|^2$ in Eq. (5) and (6). The left first and second Fano dips are originated from phonon1 and phonon2 dressing. The central Fano dip is resulted from photon1

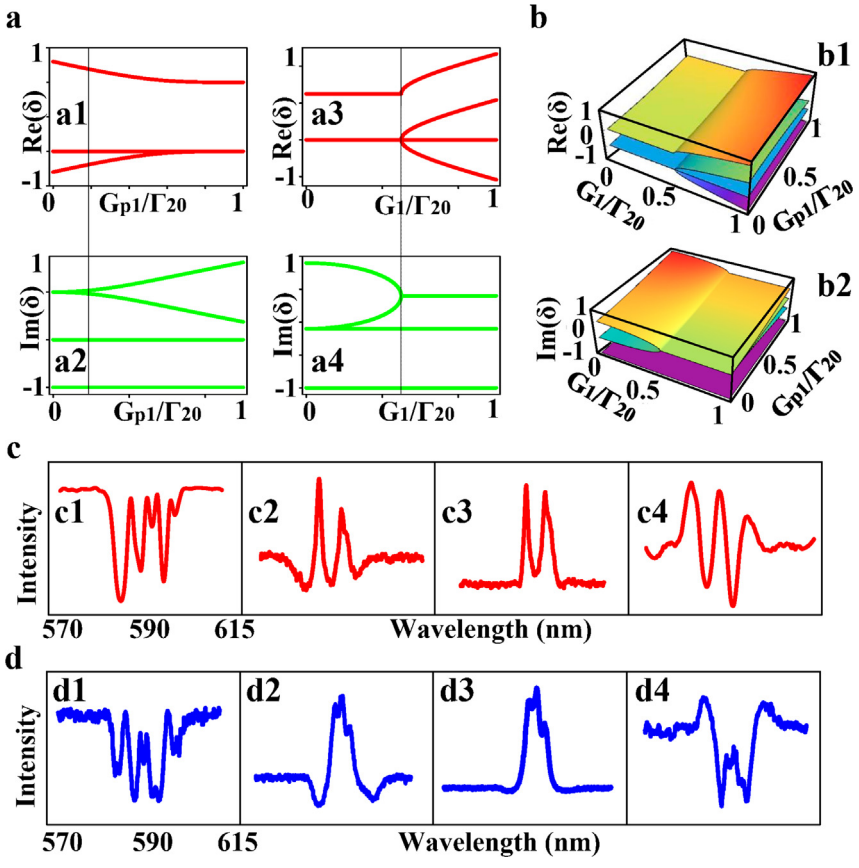

Fig. 6 | Theoretical and experimental EP. **a,** Real and a(a2, a4), imaginary parts of the eigenvalues as a function of the dressing Rabi frequency (G) and transverse dephase rate (Γ) with a Gaussian-likeenvelope. **b,** 3D simulation corresponding to 2D simulation a1−a2, a3−a4, respectively. The spectral signal measured at PMT2 obtained from **c, d**; (0.5 : 1) sample of Eu^{3+} : $BiPO_4$ and Eu^{3+} : $NaYF_4$ when E_1 is scanned from 572.4 nm to 612.4 nm and GP is changed **c,** (500 μs, 2 ms, 5 ms, 20 ms) and **d,** (1 ms, 6 ms, 10 ms, 25 ms) at 200 ns gate width and 300 K temperature at power = 9 mW, respectively. Abbreviation: PMT, photomultiplier tube; 2D, two-dimensional; 3D, three-dimensional.

dressing. The fourth and fifth Fano dips can be explained by phonon3 and phonon4 dressing. Compared to the other four Fano dips, the fifth Fano dip is the strongest (Fig. 4a4) due to photon dressing (similar to Fig. 4c1, c2 and Fig. 5a1, b1).

With the GP reaching 5 ms, the two sharp peaks can be observed in Fig. 6c3 corresponding to EP, where G and Γ are equal due to the dominance of CF splitting (Fig. 1a2), which is validated by theoretical results in Fig. 6a. The visible three Fano dips observed in Fig. 2a12, Fig. 4a2, b2, and Fig. 6c3 are attributed to the stronger nested three dressing (photon1−phonon1−phonon2 atomic coherence coupling in Fig. 1a4) than CF splitting. The evolution from three Fano dips to two sharp EP peaks to five Fano dips is corresponding to Fig. 1a2, a4, Fig. 6b1, b2 are the three-dimensional simulation results corresponding to the real and imaginary parts of 2D simulations (Fig. 6a,b), respectively.

Lastly, Fig. 6c exhibits fourth-order (N = 3) at $^{7}F_{1,\ MJ\ =\ \pm1}$, which corresponds to four eigenvalues in a univariate quartic with three dressing, and one third-order (N = 2) EP control at $^{7}F_{1,\ MJ\ =\ \pm1}$ corresponding to four eigenvalues in a univariate cubic equation (S3 Galois group) with two dressing for left and right peaks, respectively. Fig. 6d1−d4 exhibits one third-order (N = 2) EP control for each peak.

CONCLUSION

In summary, this research examined the phenomenon of multi-Fano dips and demonstrated that their behavior can be regulated by higher-order EPs control in non-Hermitian systems. Additionally, the relationship between multi-Fano interference and the photon−phonon nested dressing effect was demonstrated for various Eu^{3+} : $BiPO_4$ samples. This research established the categorization of the multi-Fano resonance between discrete and continuous states into three distinct types (dressed FL, hybrid, and dressed SFWM Fano interference), which can be controlled through the GP (ratio of FL and Stokes). Moreover, the experimental results suggest a scheme for achieving a higher channel equalization ratio of about 80%.

METHODS

Experimental setup The samples were held in a cryostat with different temperatures. Two dye lasers were used to generate the two pumping fields. The spectral optical outputs are obtained by scanning laser frequency, while the temporal optical outputs are fixed by DL frequency. The optical signal generated is detected at PMT. The ratio of FL to ES/AS is changed by different gate positions. Moreover, The point group site symmetry of different phases of samples can control multi-Fano resonance.

REFERENCES

1. Fano, U. Effects of configuration interaction on intensities and phase shifts. *Phys. Rev.* **124**, 1866 (1961). https://doi.org/10.1103/PhysRev.124.1866.
2. Limonov, M. F., Rybin, M. V., Poddubny, A. N. & Kivshar, Y. S. Fano resonances in photonics. *Nat. Photonics* **11**, 543−554 (2017). https://doi.org/10.1038/nphoton.2017.142.
3. Lalanne, P., Yan, W., Vynck, K., Sauvan, C. & Hugonin, J.-P. Light interaction with photonic and plasmonic resonances. *Laser Photon. Rev.* **12**, 1700113 (2018). https://doi.org/10.1002/lpor.201700113.
4. Lim, W. X., Manjappa, M., Pitchappa, P. & Singh, R. Shaping high-*Q* planar Fano resonant metamaterials toward futuristic technologies. *Adv. Opt. Mater.* **6**, 1800502 (2018). https://doi.org/10.1002/adom.201800502.
5. Kroner, M. et al. The nonlinear Fano effect. *Nature* **451**, 311−314 (2008). https://doi.org/10.1038/nature06506.
6. Ott, C. et al. Lorentz meets Fano in spectral line shapes: a universal phase and its laser control. *Science* **340**, 716−720 (2013). https://doi.org/10.1126/science.1234407.
7. Stockman, M. I. Dark-hot resonances. *Nature* **467**, 541−542 (2010). https://doi.org/10.1038/467541a.
8. Limonov, M. F. Fano resonance for applications. *Adv. Opt. Photonics* **13**, 703−771 (2021). https://doi.org/10.1364/AOP.420731.
9. Beutler, H. Über Absorptionsserien von Argon, Krypton und Xenon zu Termen zwischen den beiden beiden Ionisierungsgrenzen $^{2}P^{2/0}{}_{3}$ und $^{2}P^{2/0}{}_{1}$. *Z. Phys.* **93**, 177−196 (1935). https://doi.org/10.1007/BF01365116.
10. Sorensen, S. L. et al. Argon 3s autoionization resonances. *Phys. Rev. A* **50**, 1218 (1994). https://doi.org/10.1103/PhysRevA.50.1218.
11. Hodaei, H. et al. Enhanced sensitivity at higher-order exceptional points. *Nature* **548**, 187−191 (2017). https://doi.org/10.1038/nature23280.
12. Wang, Y. et al. Manipulating cavity photon dynamics by topologically curved space. *Light: Sci. Appl.* **11**, 308 (2022). https://doi.org/10.1038/s41377-022-01009-x.
13. Ren, B. et al. Observation of nonlinear disclination states. *Light: Sci. Appl.* **12**, 194 (2023). https://doi.org/10.1038/s41377-023-01235-x.
14. Miri, M.-A. & ALÙ, A. Exceptional points in optics and photonics. *Science* **363**, eaar7709 (2019). https://doi.org/10.1126/science.aar7709.
15. Wu, H. et al. Fundamental distinction of electromagnetically induced transparency and Autler-Townes splitting in breaking the time-reversal symmetry. *Laser Photon. Rev.* **16**, 2100708 (2022). https://doi.org/10.1002/lpor.202100708.
16. Midya, B., Zhao, H. & Feng, L. Non-Hermitian photonics promises exceptional topology of light. *Nat. Commun.* **9**, 2674 (2018). https://doi.org/10.1038/s41467-018-05175-8.
17. Zhu, D., Liu, S., Fan, R., Xiao, S. M. & Song, Q. Unidirectional emission from a PT-symmetric annular microcavity. *Phys. Rev. A* **99**, 033849 (2019). https://doi.org/10.1103/PhysRevA.99.033849.
18. Zhang, Z. et al. Parity-time-symmetric optical lattice with alternating Gain and loss atomic configurations. *Laser Photon. Rev.* **12**, 1800155 (2018). https://doi.org/10.1002/lpor.201800155.
19. Krasnok, A., Tymchenko, M. & Alù, A. Nonlinear metasurfaces: a paradigm shift in nonlinear optics. *Mater. Today* **21**, 8−21 (2018). https://doi.org/10.1016/j.mattod.2017.06.007.
20. Koshelev, K. et al. Subwavelength dielectric resonators for nonlinear nanophotonics. *Science* **367**, 288−292 (2020). https://doi.org/10.1126/science.aaz3985.
21. Liang, G. et al. Mid-infrared photonics and optoelectronics in 2D materials. *Mater. Today* **51**, 294−316 (2021). https://doi.org/10.1016/j.mattod.2021.09.021.
22. Safavi-Naeini, A. H. et al. Electromagnetically induced transparency and slow light with optomechanics. *Nature* **472**, 69−73 (2011). https://doi.org/10.1038/nature09933.
23. Kim, Y. & Lee, J. D. Ultrafast dynamics of phase and topology in Dirac semiconductors. *Mater. Today Phys.* **21**, 100525 (2021). https://doi.org/10.1016/j.mtphys.2021.100525.
24. Zhen, B. et al. Enabling enhanced emission and low-threshold lasing of organic molecules using special Fano resonances of macroscopic photonic crystals. *PANS* **110**, 13711−13716 (2013). https://doi.org/10.1073/pnas.1311866110.
25. Yu, Y., Xue, W., Semenova, E., Yvind, K. & Mork, J. Demonstration of a self-pulsing photonic crystal Fano laser. *Nat. Photonics* **11**, 81−84 (2017). https://doi.org/10.1038/nphoton.2016.248.
26. Lu, C.-C. et al. On-chip topological nanophotonic devices. *Chip* **1**, 100025 (2022). https://doi.org/10.1016/j.chip.2022.100025.
27. Tian, Z.-N. et al. On-chip single-photon chirality encircling exceptional points. *Chip* **2**, 100066 (2023). https://doi.org/10.1016/j.chip.2023.100066.
28. Streubel, R., Barcikowski, S. & Gökce, B. Continuous multigram nanoparticle synthesis by high-power, high-repetition-rate ultrafast laser ablation in liquids. *Opt. Lett.* **41**, 1486−1489 (2016). https://doi.org/10.1364/OL.41.001486.
29. Raza, F. Multi-channel router and logic NAND gate from multiple Autler-Townes splitting controlled by phase transition. *RSC Adv.* **10**, 15239−15244 (2020). https://doi.org/10.1039/D0RA01379J.
30. Romero, B., Bruque, S., Aranda, M.A. G. & Iglesias, J. E. Syntheses, crystal structure, and characterization of bismuth phosphates. *Inorg. Chem.* **33**, 1869−1874 (1994). https://doi.org/10.1021/ic00087a023.
31. Serrano, D. et al. Ultra-narrow optical linewidths in rare-earth molecular crystals. *Nature* **603**, 241−246 (2022). https://doi.org/10.1038/s41586-021-04316-2.

32. Zhong, T. et al. Nanophotonic rare-earth quantum memory with optically controlled retrieval. *Science* **357**, 1392−1395 (2017). https://doi.org/10.1126/science.aan5959.
33. Ma, Y., Ma, Y.-Z., Zhou, Z.-Q., Li, C.-F. & Guo, J.-C. One-hour coherent optical storage in an atomic frequency comb memory. *Nat. Commun.* **12**, 2381 (2021). https://doi.org/10.1038/s41467-021-22706-y.
34. Mooney-Slater, R. C. L. Polymorphic of bismuth phosphate. *Z. für Krist. - Cryst. Mater.* **117**, 371−385 (1962). https://doi.org/10.1524/zkri.1962.117.16.371.
35. Li, J. et al. Superior atomic coherence time controlled by crystal phase transition and optical dressing. *Opt. Lett.* **47**, 2310−2313 (2022). https://doi.org/10.1364/OL.446322.
36. Fan, H. et al. Photon-phonon atomic coherence interaction of non-linear signals in various phase transitions Eu^{3+}: $BiPO_4$. *Nanomaterials* **12**, 4304 (2022). https://doi.org/10.3390/nano12234304.
37. Zhao, Y. et al. Temporal interaction of hybrid signals in various phases of Eu^{3+}: $BiPO_4$ through photonphonon dressing. *New J. Phys.* **24**, 083037 (2022). https://doi.org/10.1088/1367-2630/ac88ed.
38. Li, P. et al. Orthogonally polarized luminescence of single bismuth phosphate microcrystal doped with europium. *Adv. Opt. Mater.* **8**, 2000583 (2020). https://doi.org/10.1002/adom.202000583.
39. Li, P. et al. Deterministic relation between optical polarization and lattice symmetry revealed in ion-doped single microcrystals. *ACS Nano* **16**, 9535−9545 (2022). https://doi.org/10.1021/acsnano.2c02756.
40. Li, P. et al. Phase control of Eu^{3+}-doped YPO_4 nano/microcrystals. *Cryst. Growth Des.* **17**, 5935−5944 (2017). https://doi.org/10.1021/acs.cgd.7b01038.
41. Li, P., Yuan, T., Li, F. & Zhang, Y. Phosphate ion-driven $BiPO_4$: Eu phase transition. *J. Phys. Chem. C* **123**, 4424−4432 (2019). https://doi.org/10.1021/acs.jpcc.8b10410.
42. Liu, Y., Tu, D., Zhu, H. & Chen, X. Lanthaide-doped luminescent nanoprobes: controlled synthesis, optical spectroscopy, and bioapplications. *Chem. Soc. Rev.* **42**, 6924−6958 (2013). https://doi.org/10.1039/C3CS60060B.

MISCELLANEA

Supplementary materials Supplementary data to this article can be found online at https://doi.org/10.1016/j.chip.2023.100077.

Funding This work was supported by the National Key Research and Development Program of China (2017YFA0303700, 2018YFA0307500), Key Scientific and Technological Innovation Team of Shaanxi Province (2021TD-56), and National Natural Science Foundation of China (61975159, 11904279, 12174302, 62022066, 12074306, 12074303).

Declaration of Competing Interest The authors declare no competing interests.